

Local Structure and Density of Liquid Fe-C-S Alloys at Moon's Core Conditions



Key Points:

- We measured the local structure and density of liquid Fe-C-S alloys in the range of 1–5 GPa and 1600–1900 K
- A thermodynamic model based on asymmetric Margules formalism was built based on this data set
- We used this thermodynamic model to address three of the latest models of the Moon's core and to discuss the possible C and S content

Bin Zhao¹ , Guillaume Morard² , Eglantine Boulard¹, Silvia Boccato¹, Nicki C. Siersch¹, Attilio Rivoldini³ , Nicolas Guignot⁴, Laura Henry⁴, Andrew King⁴, Claire Zurkowski⁵ , Yingwei Fei⁵ , and Daniele Antonangeli¹

¹Muséum National d'Histoire Naturelle, UMR CNRS 7590, Institut de Minéralogie, de Physique des Matériaux et de Cosmochimie, IMPMC, Sorbonne Université, Paris, France, ²CNRS, IRD, ISTERRE, Université Gustave Eiffel, Université Grenoble Alpes, Université Savoie Mont Blanc, Grenoble, France, ³Royal Observatory of Belgium, Brussels, Belgium, ⁴Synchrotron SOLEIL, L'Orme de Merisiers, Gif-sur-Yvette, France, ⁵Earth and Planets Laboratory, Carnegie Institution for Science, Washington, DC, USA

Supporting Information:

Supporting Information may be found in the online version of this article.

Correspondence to:

B. Zhao,
zhaobin027@gmail.com

Citation:

Zhao, B., Morard, G., Boulard, E., Boccato, S., Siersch, N. C., Rivoldini, A., et al. (2023). Local structure and density of liquid Fe-C-S alloys at Moon's core conditions. *Journal of Geophysical Research: Planets*, 128, e2022JE007577. <https://doi.org/10.1029/2022JE007577>

Received 15 SEP 2022

Accepted 19 FEB 2023

Author Contributions:

Conceptualization: Bin Zhao, Guillaume Morard, Daniele Antonangeli

Data curation: Bin Zhao

Formal analysis: Bin Zhao

Funding acquisition: Daniele Antonangeli

Investigation: Bin Zhao, Guillaume Morard, Eglantine Boulard, Silvia Boccato, Nicki C. Siersch, Nicolas Guignot, Daniele Antonangeli

Methodology: Guillaume Morard, Eglantine Boulard, Attilio Rivoldini, Daniele Antonangeli

Project Administration: Guillaume Morard, Daniele Antonangeli

Supervision: Bin Zhao, Guillaume Morard, Daniele Antonangeli

Validation: Bin Zhao, Guillaume Morard, Daniele Antonangeli

Visualization: Bin Zhao, Guillaume Morard, Daniele Antonangeli

Writing—original draft: Bin Zhao, Guillaume Morard, Daniele Antonangeli

Writing—review and editing: Bin Zhao, Guillaume Morard, Daniele Antonangeli

Supporting Information: Bin Zhao, Guillaume Morard, Daniele Antonangeli

Conflict of Interest: None

Supporting Information: Bin Zhao, Guillaume Morard, Daniele Antonangeli

Supporting Information: Bin Zhao, Guillaume Morard, Daniele Antonangeli

Supporting Information: Bin Zhao, Guillaume Morard, Daniele Antonangeli

Supporting Information: Bin Zhao, Guillaume Morard, Daniele Antonangeli

Supporting Information: Bin Zhao, Guillaume Morard, Daniele Antonangeli

Supporting Information: Bin Zhao, Guillaume Morard, Daniele Antonangeli

Supporting Information: Bin Zhao, Guillaume Morard, Daniele Antonangeli

Supporting Information: Bin Zhao, Guillaume Morard, Daniele Antonangeli

Supporting Information: Bin Zhao, Guillaume Morard, Daniele Antonangeli

Supporting Information: Bin Zhao, Guillaume Morard, Daniele Antonangeli

Supporting Information: Bin Zhao, Guillaume Morard, Daniele Antonangeli

Supporting Information: Bin Zhao, Guillaume Morard, Daniele Antonangeli

Supporting Information: Bin Zhao, Guillaume Morard, Daniele Antonangeli

Supporting Information: Bin Zhao, Guillaume Morard, Daniele Antonangeli

Abstract The local structure and density of ternary Fe-C-S liquid alloys have been studied using a combination of in situ X-ray diffraction and absorption experiments between 1 and 5 GPa and 1600–1900 K. The addition of up to 12 at% of carbon (C) to Fe-S liquid alloys does not significantly modify the structure, which is largely controlled by the perturbation to the Fe-Fe network induced by S atoms. The liquid density determined from diffraction and/or absorption techniques allows us to build a non-ideal ternary mixing model as a function of pressure, temperature, and composition in terms of the content of alloying light elements. The composition of the Moon's core is addressed based on this thermodynamic model. Under the assumption of a homogeneous liquid core proposed by two recent Moon models, the sulfur content would be 27–36 wt% or 12–23 wt%, respectively, while the carbon content is mainly limited by the Fe-C-S miscibility gap, with an upper bound of 4.3 wt%. On the other hand, if the core is partially molten, the core temperature is necessarily lower than 1850 K estimated in the text, and the composition of both the inner and outer core would be controlled by aspects of the Fe-C-S phase diagram not yet sufficiently constrained.

Plain Language Summary Several geodetic and geochemical studies addressed the properties of the Moon's core, but its density remains poorly constrained. Core density is directly related to its chemical composition, which is crucial for better understanding Moon's origin and evolution. With carbon and sulfur being considered as two plausible light elements alloyed to iron to form the core, we selected a series of Fe-C-S compositions and studied the local structure and density of the corresponding liquids. The measured densities were integrated to build a thermodynamic model. Our results show that sulfur and carbon have a co-effect on the density and sound velocity of the liquid alloys, with sulfur playing a much more significant role. Consequently, the sulfur content is relatively well constrained for a given density, which however largely differs from model to model. On the contrary, the constraints on C content remain loose because of the smaller effect of C on the density and the inadequate knowledge of the Fe-C-S ternary phase diagram. While specific C and S ranges can be pointed out under the hypothesis of a fully molten core, the compositional constraints on a partially molten core are limited by the lack of knowledge of Fe-C-S phase diagram at pertinent conditions.

1. Introduction

Despite the large amount of seismic, geodetic, and electromagnetic data collected during the past half-century (e.g., Dickey et al., 1994; Hood et al., 1999; Konopliv et al., 1998), and the high accuracy measurements performed during the last 20 years, major questions remain open regarding the deepest regions of the Moon, especially its core (e.g., Lognonné et al., 2003; Nakamura et al., 1974; Toksöz et al., 1974). Electromagnetic sounding data from Lunar Prospector imply that the core region is metallic (Hood et al., 1999; Shimizu et al., 2013), while Apollo seismic data indicate high attenuation of acoustic waves passing through the core region (Nakamura, 2005; Weber et al., 2011). Other more specific but fundamental core properties such as size, density, and composition still remain rather uncertain (e.g., Garcia et al., 2011; Williams et al., 2014). To date, only a few consensus have been reached: (a) The core should be at least partially molten in line with the moonquake records and geodetic observations (e.g., Lognonné & Johnson, 2007); (b) The mean core density is below that of pure iron, in order to match the measured moment of inertia (e.g., Garcia et al., 2019; Viswanathan et al., 2019); (c) Light elements

© 2023. The Authors.

This is an open access article under the terms of the [Creative Commons Attribution License](https://creativecommons.org/licenses/by/4.0/), which permits use, distribution and reproduction in any medium, provided the original work is properly cited.

Resources: Nicolas Guignot, Laura Henry, Andrew King, Claire Zurkowski, Yingwei Fei
Software: Silvia Boccato, Nicolas Guignot, Laura Henry, Andrew King
Supervision: Guillaume Morard, Daniele Antonangeli
Visualization: Bin Zhao
Writing – original draft: Bin Zhao
Writing – review & editing: Bin Zhao, Guillaume Morard, Eglantine Boulard, Silvia Boccato, Nicki C. Siersch, Attilio Rivoldini, Claire Zurkowski, Yingwei Fei, Daniele Antonangeli

are needed in the core to decrease its crystallizing temperature and density (e.g., Garcia et al., 2019; Kuskov et al., 2021; Weber et al., 2011; Wieczorek et al., 2006), and sulfur is often favored as the main light element (e.g., Antonangeli et al., 2015; Jing et al., 2014; O'Neill, 1991; Weber et al., 2011). Based on joint inversion of available independent observations from Apollo missions, LLR (Lunar Laser Ranging) and GRAIL (Gravity Recovery and Interior Laboratory) data, and comparative geochemical analysis of Moon samples vs. bulk silicate Earth, several models have been put forward, which however show significant density spreading in the core, ranging from 4,200 to 7,000 kg/m³ (e.g., Garcia et al., 2011; Kuskov et al., 2021; Weber et al., 2011).

Sulfur is the most favored light element to be alloyed with iron in the Moon's core, because of its chemical affinity to iron at Moon's core conditions (siderophile behavior), and its effectiveness in decreasing the density of pure iron. In particular, considering the eutectic point of planetary-core-relevant iron alloys, the relatively low temperature of the Moon's interior (T between 1300 and 1900 K, e.g., Karato, 2013; Khan et al., 2006; Pommier et al., 2022; Wieczorek et al., 2006) points to an Fe- and S-rich core as the simplest explanation. Furthermore, the depletion of the lunar mantle in siderophile elements is possibly related to the presence of sulfur in the core (Rai & van Westrenen, 2014). Other light elements, such as oxygen and silicon, are not expected in significant concentrations as oxygen solubility into iron seems to be relatively low at the pressures pertinent to the Moon's core (Ricolleau et al., 2011), and the oxidizing conditions during the core differentiation do not favor silicon (Kilburn & Wood, 1997). On the other hand, carbon could be a potential light element component, with up to 4.8 wt% C estimated in the Moon's core lunar core, although its presence and abundance are debated (e.g., Steenstra et al., 2017 and references therein). As such, the phase diagram and the thermo-elastic properties of Fe-C and Fe-S binary liquids have been intensively studied at pressures in the range of 1–10 GPa and temperatures between 1700 and 2200 K, forming the basis for discussing implications for Moon's core composition, origin, and thermal evolution.

Sulfur strongly decreases the melting temperature, density, and sound velocity of liquid iron (see Morard et al., 2018 and references therein) at Moon's core conditions. The phase diagram of Fe-S has been studied at pertinent *P-T* conditions by analysis of recovered samples and in situ X-ray diffraction (Fei et al., 1997, 2000). Sound velocity of liquid Fe-S has been studied by ultrasonic measurements (Jing et al., 2014; Nishida et al., 2016, 2020) and molecular dynamic calculations (Kuskov & Belashchenko, 2016). Density has been studied in situ by the sink/float method, X-ray diffraction, and absorption (Morard et al., 2018; Nishida et al., 2008, 2011; Sanloup et al., 2000; Xu et al., 2021). Thermodynamic models of liquid Fe-S at Moon's core conditions based on these experimental data show a strong non-ideal mixing behavior between liquid Fe and FeS (Morard et al., 2018; Terasaki et al., 2019; Xu et al., 2021). Macroscopic properties can be related to the local structure of the liquid, that is, how the Fe and S atoms are distributed in the short-range distance. In the binary liquid, sulfur is suggested to be incorporated interstitially in liquid iron (Shibazaki & Kono, 2018). Studies indicate that a small amount of sulfur does not significantly affect the local organization of the first coordination shells of the liquid, while the structure exhibits a progressively increased disorder for S concentration above 23.5 at% and the liquid becomes poorly organized for the end member FeS (Morard et al., 2018; Shibazaki & Kono, 2018).

Carbon is also an interstitial element in liquid iron (Shibazaki & Kono, 2018). However, as carbon atoms are much smaller in size compared to sulfur atoms, their inclusion perturbs the Fe liquid structure to a much lower extent. Unlike the disordered Fe-S alloys, Fe-C liquids at high pressure maintain a relatively well-defined local structure for C concentration up to 25 at% (Fe₃C). Consequently, the density (Sanloup et al., 2011; Shimoyama et al., 2013; Terasaki et al., 2010) and sound velocity (Kuwabara et al., 2016; Shimoyama et al., 2016) of Fe-C liquids do not markedly decrease with increasing carbon content. A density discontinuity was first found in liquid Fe-5.7 wt% C around 6 GPa by Sanloup et al. (2011), and was attributed to a liquid-liquid phase transition of Fe-C at 5.2 GPa. This density discontinuity was reproduced on liquid Fe-3.5 wt% C (Shimoyama et al., 2013), and afterward, the phase transition was supported by the observation of a subtle structural change at ~5 GPa (Shibazaki et al., 2015).

While the two binary liquids have been well studied, the ternary Fe-C-S system, and in particular ternary Fe-C-S liquid alloys, remain far from being fully understood, with only a few data published on miscibility (Corgne et al., 2008; Dasgupta et al., 2009) and melting (Dasgupta et al., 2009; Deng et al., 2013). In this study, synchrotron X-ray diffraction and absorption experiments were conducted on ternary Fe-C-S liquid alloys in a Paris-Edinburgh cell up to 5 GPa and 1900 K to investigate in situ the effect of the simultaneous incorporation of carbon and sulfur on the local structure and density of liquid iron alloys. The measured density data have been

used to establish a thermodynamic model for Fe-C-S liquid solutions, which in turn can be used to help to determine the composition of the core of the Moon and other small planetary bodies.

2. Materials and Methods

2.1. Sample Preparation

Iron (99.5%, Alfa Aesar), FeS (99.98%, Alfa Aesar), and graphite powders (99%, Alfa Aesar) were grounded in an agate mortar for 30 min to produce samples of nominal compositions of Fe-1.5 wt% C-4 wt% S (hereafter referred to as Fe-1.5C-4S), Fe-1.5C-8S, Fe-1.5C-15S, Fe-1.5C-22S, Fe-1.5C-30S, Fe-3C-4S, and Fe-3C-8S. Mixed powders were dried in a vacuum stove at 150°C for 1 hr, and loaded in BN capsules (*Beamtime0720*) or sapphire rings (*Beamtime0921*), prior to the X-ray diffraction and/or absorption experiments. While X-ray diffraction measurements have been conducted in both beamtimes, X-ray absorption measurements have been performed only in *Beamtime0921*, for which the sapphire capsules have been employed.

2.2. High-Pressure In Situ X-Ray Diffraction Experiments

In situ synchrotron X-ray diffraction and absorption experiments were carried out using the newly designed UToPEC (Ultrafast Tomography Paris Edinburgh Cell) (Boulard et al., 2018) at the PSICHÉ beamline, Synchrotron SOLEIL, France. The samples were loaded into a PEC assembly (shown in Figure S2 of Supporting Information S1) consisting of a sapphire ring, a BN capsule, a graphite furnace, and a boron epoxy gasket, similar to the one reported by Boulard et al. (2020). Pressure was generated by a pair of tungsten carbide anvils driven by a hydraulic pump, while high temperature generation was ensured by the above-mentioned graphite resistive furnace. Temperature as a function of power was calibrated in a dedicated run before the experiments by a non-destructive cross-calibration method (e.g., Parker et al., 2010) using the thermal Equation of State (EOS) of Pt, hBN, and MgO (Matsui et al., 2000, 2009; Y. Zhao et al., 1997) and the unit-cell volumes determined by X-ray diffraction at each power step. The error in temperature, including possible gradients, is estimated to be ± 100 K. The hBN capsule, surrounding the sapphire ring, also served as the pressure calibrant (x-ray patterns collected on hBN close to sample are analyzed to derive volume, which in turn provide pressure by use of known thermal equation of state (Y. Zhao et al., 1997)). The high brilliance polychromatic X-ray beam with energy ranging from 10 to 90 keV was collimated to $25 \times 50 \mu\text{m}^2$ (vertical \times horizontal FWHM) by two slits before the sample. The diffracted beam was collected by a Ge solid-state detector.

In each experiment, the sample was initially cold compressed to the target pressure, and then molten by heating up at a rate of 100 K/min. At temperatures above 1150 K (corresponding to 300 W), the different phases present in the sample were checked every 50 W by diffraction. The fully molten status of the sample was pinpointed by the absence of sharp diffraction peaks of solids on top of the diffuse scattering signal from the liquid, and further confirmed by tomography. Indeed, thanks to the fast computed-tomography capabilities available at the PSICHÉ beamline (Boulard et al., 2018), the status of samples can also be monitored by 3D tomography images. Figure S3 in Supporting Information S1 shows the sequence obtained by increasing the temperature from solid powder mixture to fully molten sample. We note that ternary alloy with high light element content at low pressure (< 3 GPa) proved to be immiscible, hence only high-pressure data were collected for the sulfur-rich samples. Once fully molten, a CAESAR (Combined Angle and Energy Dispersive Structure Analysis and Refinement) scan was collected by combining the recorded energy-dispersive diffraction pattern at angles from $2\theta = 2.5^\circ$ – 29.5° with a step of 0.2° (King et al., 2022). The counting times for $2\theta = 2.5$ – 10° , 10 – 20° , and 20 – 29.5° ranges were respectively 5, 10, and 20 s, for a total duration of the whole scan of about 20 min. The combined energy and 2θ ranges enable a data collection over an extended wave vector (Q), up to 20 \AA^{-1} . A preset function controlled the motion of slits in front of the Ge detector and ensured signal collection from a fixed and constant volume of the sample irrespective of the angle.

The CAESAR data were analyzed on the basis of the methodology developed by Eggert et al. (2002) and Morard et al. (2014) implemented into the software AMORPHEUS (Boccatto et al., 2022) to study the local structure and density of the liquids. In particular, the pair distribution function $g(r)$ and distribution function $F(r)$ (also referred to as reduced distribution function) are obtained from the collected $S(Q)$ by a Fourier transformation. For $r < r_{\min}$ $F(r) = -4\pi r \rho$, where r_{\min} is the minimum distance between two atoms due to the interatomic repulsive force, and ρ the atomic density. A figure of merit χ^2 as a function of r_{\min} is defined to minimize the oscillation of $F(r)$ in

the low r region. When χ^2 reaches the local minimum, the atomic density ρ is determined by the slope of $F(r)$ over $r < r_{\min}$. The error on atomic density obtained by this method is empirically estimated by considering the effects on the resulting density due to the selected Q range, the self-absorption from the sample, and the scattering background residual from the surrounding materials and resulted in ± 3 atoms/nm³, in line with what previously reported in similar work (Morard et al., 2014). For materials of present interest, this yields an uncertainty on density of about ± 250 kg/m³.

2.3. High-Pressure In Situ X-Ray Absorption Experiments

Predefined routines allow rapid commuting of the beamline setup from diffraction mode to absorption mode while sharing the same general optics layout. Absorption profiles were thus collected right after each diffraction acquisition. In this configuration, the size of the incident beam was reduced to $10 \times 10 \mu\text{m}^2$ (vertical \times horizontal FWHM) by collimating slits. An MgO polycrystalline sample was added to the optical path, between the sample and the detector, to act as a polychromator. On the downstream side, the detector was fixed at 8° with respect to the straight beam path, and the two diffraction peaks of MgO located at 37.5 keV (200) and 53.5 keV (220) were employed to record the absorption profile while scanning the sample (the intensities of the diffraction peaks are proportional to the beam intensity transmitted across the sample). Reference incident intensity was measured by translating the sample completely out of the beam. The detailed experimental procedure was described by Henry et al. (2022). One of the main advantages of this setup is that no extra optical paths or detectors were needed, and the absorption profile of the assembly was taken at the same experimental condition as the CAESAR scan.

Based on the Beer–Lambert law, it was possible to extract from the absorption profile the value of $(\mu\rho)_{P,T}$, the product of mass absorption coefficient and density at experimental P-T conditions. In order to disentangle the density from the absorption coefficient, we assumed the liquid to have the same absorption coefficient of the hot solid, which, in turn, is obtained from the absorption profile collected on the solid just before melting, imposing the density ρ_S inferred from energy-dispersive X-ray diffraction:

$$\rho_{P,T} = \frac{(\mu\rho)_{P,T}}{(\mu\rho)_S/\rho_S} \quad (1)$$

The details of data processing for diffraction and absorption can be found in Supporting Information S1.

3. Results

3.1. Liquid Structure

Figure 1a shows the pair correlation function $g(r)$ (or radial distribution function for isotropic media such as the liquids of the present study) together with partial $g(r)$ from calculations available in the literature. Oscillations in the $g(r)$ s become less pronounced for samples with 22.1 at% S or more, consistent with previous studies on Fe-S binary liquids (Morard et al., 2018; Shibasaki & Kono, 2018; Xu et al., 2021), in which the liquids were reported to show a more disordered structure for the S content of 23.5 at% S, 29.4 at% S, and 25.1 at% S, respectively. On the other hand, the inclusion of up to 18 at% of carbon in the ternary liquid seems not to have a detectable impact on the local structure as signatures of the second and third coordination shells are still distinguishable. The modification of the structure is controlled by the interstitial inclusion of more massive S atoms that perturb the Fe-Fe network, while smaller C atoms can enter interstitial sites between Fe atoms without significant effect on the local structure. This is further supported by the variation in the atomic density shown in Figure S4 of Supporting Information S1. The atomic density with increasing S or C content shows opposite trends, highlighting the different effect of sulfur and carbon, while the atomic density of Fe-Si liquids does not significantly change with Si content, as Si atoms substitute iron atoms.

The most prominent feature in the $g(r)$ is the position (r_1) and intensity of the first peak corresponding to the first coordination sphere. r_1 as a function of total light element content is plotted in Figure 1b and compared with results from literature obtained for binary liquids. Within the experimental uncertainties the r_1 value of Fe-S liquids is not observed to vary with S content for S addition up to ~ 20 – 25 at%, while it significantly decreases for higher concentration. As suggested by the calculated partial $g(r)$, this is likely due to the increased contribution of the shorter and covalent Fe-S bonds (Figure 1a). Since the scattering intensity is proportional to the square of the atomic number, the contribution from Fe-Fe and Fe-S bonds in the case of $\text{Fe}_{66.7}\text{C}_{11.2}\text{S}_{22.1}$ account, respectively, for $\sim 65\%$ and $\sim 27\%$ of the total signal (see Morard et al., 2008 and references therein), while the contribution from other bonds is negligible. Therefore, the formation of shorter Fe-S bonds moves the first peak position of the total $g(r)$ toward lower r value,

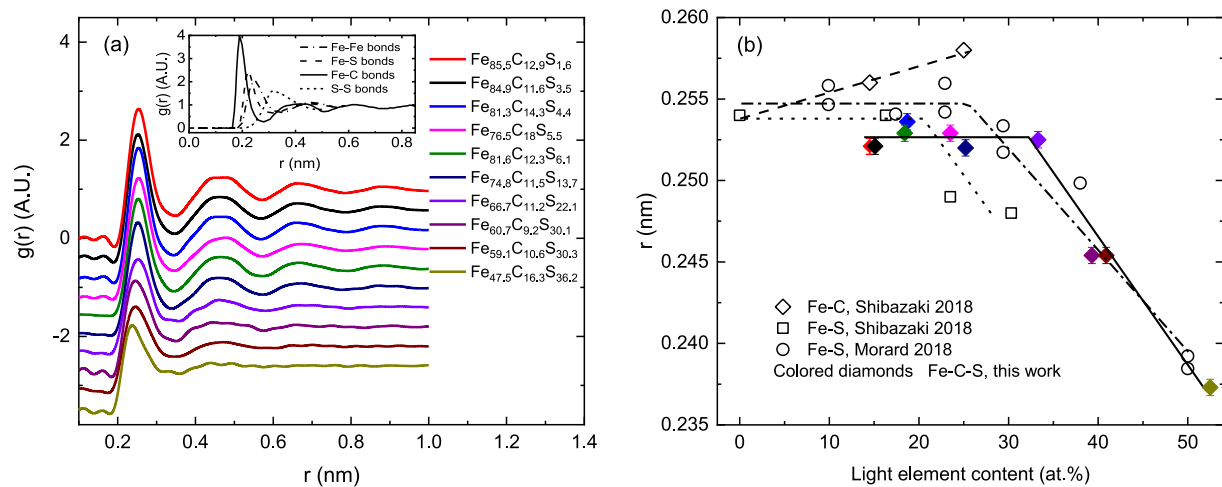


Figure 1. (a) Radial distribution function measured for Fe-C-S ternary liquids in the 1–5 GPa and 1700–1900 K range. Data are shown for increasing sulfur content (from the top to bottom). Inset: the partial $g(r)$ showing the individual contribution of Fe-Fe, Fe-S, and S-S bonds, calculated for a binary Fe-S liquid alloy with 23 at% S (Morard et al., 2018), and the partial $g(r)$ illustrating the Fe-C bonds calculated for a binary Fe-C alloy with 20 at% C (Lai et al., 2017). (b) First peak positions of the ternary alloys in comparison with results obtained for binary Fe-C and Fe-S at similar P - T condition (1.5–5.2 GPa and 1600–1980 K in Morard et al. (2018), and 3–5 GPa, 1600–2000 K in Shibazaki and Kono (2018)).

while other bonds hardly have any visible effect. For binary Fe-C liquids, the addition of carbon seems to move r_1 toward higher values according to available experimental data (Shibazaki & Kono, 2018), in apparent contrast with molecular dynamic calculations that indicate short Fe-C bonds (Lai et al., 2017). This discrepancy may imply that the addition of carbon might have a more complex perturbation effect other than simply forming the Fe-C bonds.

Our results of r_1 as a function of total light element content follow a trend qualitatively similar to that reported for the binary Fe-S by Morard et al. (2018) and Shibazaki and Kono (2018), with a closer agreement with values reported in the former. The r_1 values of Fe-C-S liquids are not affected by the light element content in the alloy if below a critical amount of about 35 at%, above that value r_1 decreases with increasing light element content. Up to 18 at% of C does not modify the two-regime behavior observed for binary Fe-S liquid alloys nor the light element threshold defining the change in the regime. Thus, in this context, C seems to play the same role as S in decreasing the r_1 value, in agreement with the length of the calculated Fe-C bonds (Lai et al., 2017), but in apparent contrast with the experimental r_1 value reported for the Fe-C liquids (Shibazaki & Kono, 2018).

3.2. Density

Table 1 summarizes the densities measured under the experimental conditions. Absorption measurements were conducted only in the second of the two synchrotron beamtimes (*Beamtime0922*). Densities obtained by diffraction and absorption are consistent, with good agreement in the cases of S-rich samples (e.g., measurements on $\text{Fe}_{60.7}\text{C}_{9.2}\text{S}_{30.1}$ and $\text{Fe}_{47.5}\text{C}_{16.3}\text{S}_{36.2}$), and the difference for measurements even on $\text{Fe}_{74.8}\text{C}_{11.5}\text{S}_{13.7}$ is smaller than 8% between the two methods. When the two methods yield slightly dissimilar results, densities measured by diffraction are systematically lower than those measured by absorption. A possible reason is that the collected diffraction signal is contributed from a sulfur-rich portion of the sample. In fact, the diffraction method would be more sensitive to local inhomogeneity compared to absorption if the diffracting volume is comparable in scale to the size of inhomogeneous regions (a few tens of microns). On the other hand, as the absorption profile is taken on the whole sample, the error from local inhomogeneity has been almost eliminated (i.e., the massive absorption coefficient is averaged). Finally, and irrespective of the above consideration, we note that both values are used to calibrate parameters of the thermodynamic model.

3.3. Thermodynamic Model

A thermodynamic solution model of the Fe-C-S liquid was built based on the thermal EOSs of the end members, Fe, FeS, and Fe_3C (parameters provided in Table S2 of Supporting Information S1) with their interactions modeled by an asymmetric Margules formulation (see Text S4 and Table S2 in Supporting Information S1; please refer to Tsuno et al. (2011) for more details on the formalism).

Table 1
Sample Composition, Experimental P-T Conditions, Measured Density, and Density Rescaled to 1850 K for Both Diffraction and Absorption Experiments

Atomic proportion (%)			Exp. T (K)	Pressure (GPa)	ρ by diffraction (kg/m ³) ^a	ρ rescaled to 1850 K (kg/m ³)	ρ by absorption (kg/m ³) ^b	ρ rescaled to 1850 K (kg/m ³)
Fe	C	S						
Beamtime0720								
84.9	11.6	3.5	1895	2.15	6,780	6,800(250)	/	/
85.5	12.9	1.6	1690	1.06	6,900	6,800(250)	/	/
81.3	14.3	4.4	1722	2.29	6,740	6,680(250)	/	/
			1895	2.09	6,600	6,620(250)	/	/
76.5	18.0	5.5	1625	2.52	6,590	6,490(250)	/	/
			1895	2.17	6,430	6,460(250)	/	/
Beamtime0921								
81.6	12.3	6.1	1760	3.86	6,550	6,510(250)	6,830	6,790(100)
			1850	3.70	6,460	6,460(250)	6,460	6,460(100)
74.8	11.5	13.7	1610	4.92	6,200	6,110(260)	6,710	6,610(110)
			1720	4.70	6,180	6,130(260)	6,630	6,570(110)
			1805	4.57	6,110	6,100(260)	6,550	6,530(110)
66.7	11.2	22.1	1760	3.72	/	/	5,950	5,920(110)
			1850	3.62	5,620	5,620(270)	6,030	6,030(110)
59.1	10.6	30.3	1760	3.44	5,020	4,990(280)	5,220	5,200(120)
			1850	3.31	5,160	5,160(280)	5,200	5,200(120)
60.7	9.2	30.1	1760	4.76	/	/	5,590	5,560(120)
			1850	4.35	5,550	5,550(280)	5,510	5,510(120)
47.5	16.3	36.2	1760	4.7	/	/	5,140	5,110(120)
			1850	4.42	4,970	4,970(280)	5,060	5,060(120)

^aUncertainty on density by XRD is ± 250 kg/m³ (see Section 2.2). ^bUncertainty on density by absorption method is ± 100 kg/m³, considering the non-uniform effect of the environment and the fitting process (see Text S3 in Supporting Information S1).

The fitted parameters to all the experimental data are listed in Table 2. Based on Equation S14 in Supporting Information S1, all relevant thermodynamic properties of Fe-C-S solutions can be computed from standard thermodynamic relations. The thermal expansion coefficients of each composition can be calculated according to its definition:

$$\alpha = \left(\frac{1}{V}\right) \left(\frac{\partial V}{\partial T}\right) \quad (2)$$

Table 2
Fitted Interaction Margules Parameters

$W_{V,Fe-Fe_3C}$	0.2 ± 0.2
W_{V,Fe_3C-Fe}	0 ± 0.2
$W_{V,Fe-FeS}$	-2.2 ± 0.4
$W_{V,FeS-Fe}$	-1.0 ± 0.4
W_{V,Fe_3C-FeS}	-3.0 ± 0.2
$W_{V,FeS-Fe_3C}$	0.8 ± 0.2

Note. All the parameters are in cm³/mol.

For comparison, the density measured at different temperature conditions are rescaled at the reference value of 1850 K by making use of the thermal expansion coefficients (Table 1), and the comparisons between ideal and non-ideal models are shown in Figure 2. The fitted Margules parameters for Fe and Fe₃C are close to 0, indicating that Fe and Fe₃C mix almost ideally at here-considered conditions. Comparing to the ideal mixing model in Figure 2a, the densities provided by Margules model in Figure 2b are in overall better agreement with the experimental data. Finally, we stress that although the here-established mixing model well accounts for the available experimental data and is suitable for density calculations for the Fe-C-S liquid system as a function of pressure and/or composition in the 0–5 GPa

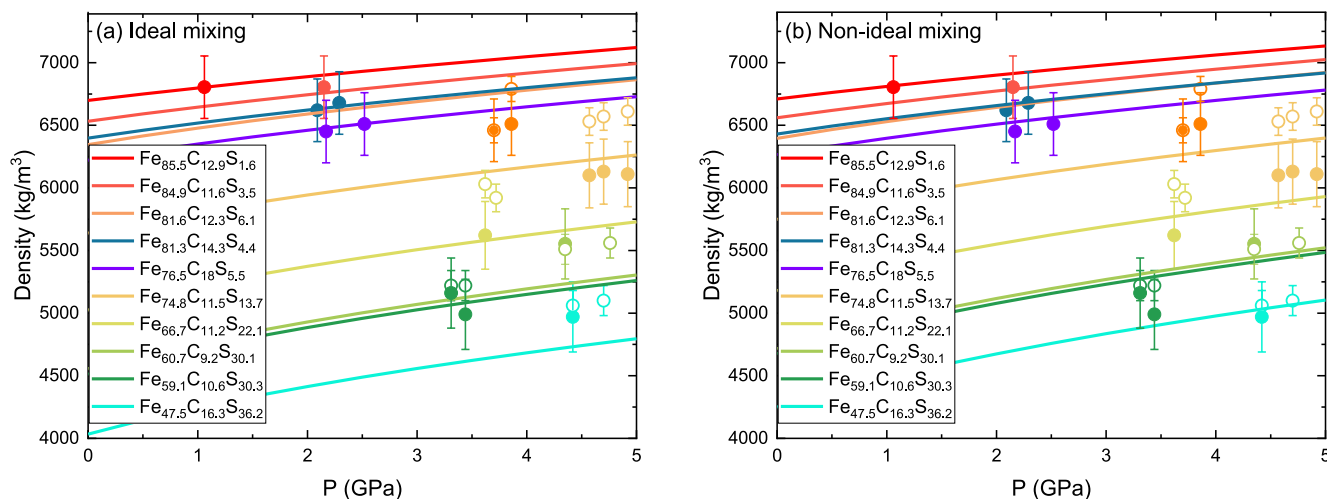


Figure 2. Density at 1850 K computed for selected compositions in the liquid Fe-C-S ternary system according to ideal (a) and non-ideal (b) thermodynamic models. (a) Ideal mixing model constructed based on the properties of Fe, Fe₃C, and FeS end members (Table S2 in Supporting Information S1). (b) Non-ideal mixing model based on the Margules mixing rule. Open circles and filled circles are results from absorption and diffraction measurements, respectively. The experimental uncertainties are mainly from the limited Q range, self-absorption, and r_{\min} fluctuation in the case of diffraction, and from minor sample deformation and fitting procedure for absorption.

range, it may no longer be valid at higher pressure, since the density discontinuity of Fe-C liquid is due to a phase transition at 5.2 GPa (Sanloup et al., 2000).

The density calculated for the liquid Fe-C-S ternary alloys at 5 GPa as a function of the light element content is shown in Figure 3a and compared with data for binary Fe-S and Fe-C alloys from literature. The uncertainties are from the fitting of the Margules parameters, which yielded $\pm 35 - \pm 75 \text{ kg/m}^3$ on the density. The most recent studies on Fe-S liquid by diffraction (Morard et al., 2018) and absorption (Terasaki et al., 2019) are in good agreement and provide higher density compared to earlier studies (Sanloup et al., 2000), while results on Fe-C liquid by absorption are all within mutual uncertainties (Sanloup et al., 2011; Shimoyama et al., 2013; Terasaki et al., 2010). The density of Fe-C-S alloy plots in between those of binary alloys, indicating a co-effect of sulfur and carbon in decreasing the density of pure iron. As alloys with high light element content reach the miscibility limit at low pressure (see Dasgupta et al., 2009), the carbon content considered in this study is restricted to less

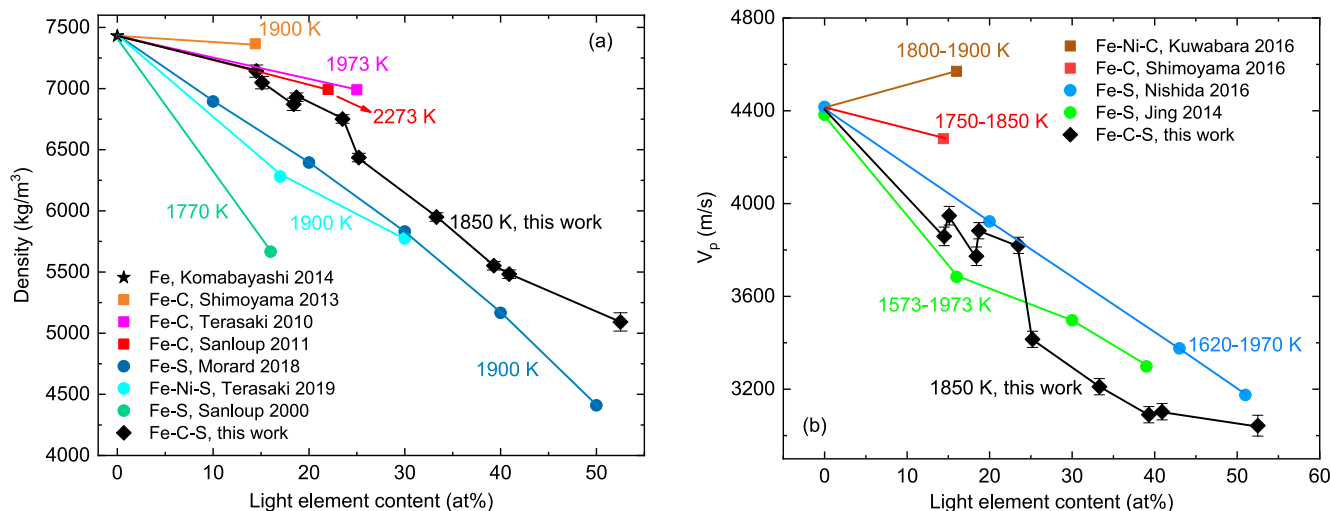


Figure 3. (a) Density and (b) sound velocity at 5 GPa modeled for the ternary Fe-C-S alloys as a function of light element content and compared with data for the binary Fe-S and Fe-C system. The reference temperature for our model is 1850 K, while the temperature of other studies is annotated adjacent to the data with the same color. Shown uncertainties on modeled properties account for uncertainties on used thermo-elastic parameters and errors on the fitting process. Lines across the points are guides for the eye.

than 18 at% to model a homogeneous ternary liquid. The density is thus largely controlled by the sulfur content, with the effect due to carbon inclusion minor as the direct consequence of the limited proportion of carbon in the modeled alloys.

3.4. Sound Velocity Calculation

The compressional sound velocity of the 10 compositions investigated in this study can be calculated at 5 GPa and 1850 K in an internally consistent way based on our thermodynamic model, following the equation

$$v_p = \sqrt{\frac{K_T(1 + \alpha\gamma T)}{\rho}} \quad (3)$$

where γ is the Grüneisen parameter, α the thermal expansion coefficient calculated by Equation 2, ρ the extrapolated density of the ternary alloy by the mixing model, and K_T the isothermal bulk modulus calculated by its definition and the mixing model, Equation S14 in Supporting Information S1:

$$K_{1850K,P} = \left[-V \left(\frac{dP}{dV} \right) \right]_{1850K} \quad (4)$$

Since there is no experimentally determined γ for Fe-S, Fe-C, or Fe-C-S, the γ of ternary Fe-C-S samples are calculated as:

$$\gamma = \frac{K_T V \alpha}{C_P - K_T V T \alpha^2} \quad (5)$$

where the C_P is the heat capacity at constant pressure of the ternary alloys, determined by the values of all the end members:

$$C_P = \frac{\partial \left(\sum_i x_i Q_i \right)}{\partial T} = \sum_i x_i C_{P,i} \quad (6)$$

where Q is the amount of heat and the subscript i represent each end members. The C_P of Fe, FeS, and Fe₃C are calculated with Equation 5 using the parameters provided in Table S2 of Supporting Information S1. The calculated thermo-elastic properties are provided in Table S3 of Supporting Information S1.

Here, we note that using other parameterizations of the bulk modulus of the alloys (e.g., Chen et al., 2014; Morard et al., 2018) and/or a value of $\gamma = 1.72$ (e.g., Kuwabara et al., 2016; Shimoyama et al., 2016) fixed to that experimentally determined for liquid Fe (Anderson & Ahrens, 1994) lead to a ~15% higher compressibility, and consequently higher velocities, without modifying the reported trend.

Figure 3b shows the calculated sound velocity compared with the data from literature for the Fe-S and Fe-C binary systems. The errors are from the fitting of Margules parameters and the uncertainties of γ . The ternary data show some scatter but follow the trend defined for Fe-S alloys. We also note that the points showing higher values of sound velocity with respect to a linear trend are those with a larger C fraction (e.g., the point at $x = 23.5$, for which C content is 18 at%). While it is difficult to independently address the effect of S and C on velocities, the sound velocity of the liquid ternary alloy would offer a useful reference to model seismic velocities in the Moon's core.

4. Discussion

The absence of data on the ternary Fe-C-S system so far has largely limited the discussion and the models of the Moon's core to the binary Fe-S and Fe-C systems, or the ternary system with Ni, which only marginally affect the thermo-elastic properties of the alloy (e.g., Antonangeli et al., 2015; Jing et al., 2014; Morard et al., 2018; Nishida et al., 2011; Terasaki et al., 2019). The current data set allows a step forward. The local structure of ternary Fe-C-S liquid here experimentally determined for the first time show that the shape of the $g(r)$ and in particular the position of the first coordination sphere evolves with increasing light element content following the

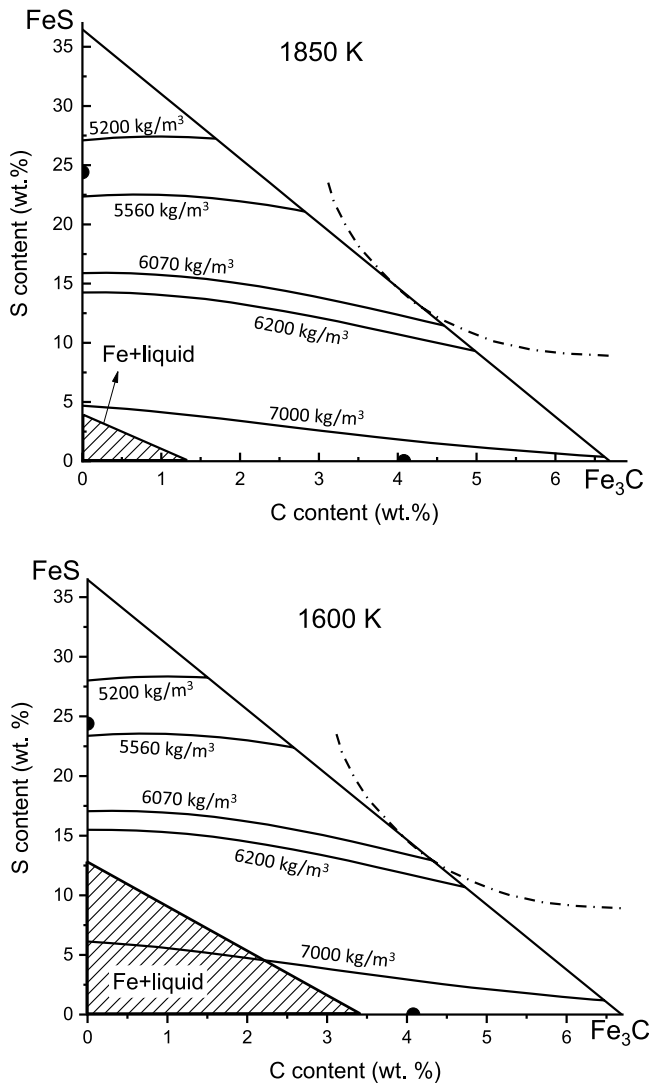


Figure 4. The carbon and sulfur content distribution within the liquid (outer) core assumed at 5 GPa and either 1850 K (top) or 1600 K (bottom) having density according to three recent Moon models: Garcia19 (Garcia et al., 2019), Viswanathan19 (Viswanathan et al., 2019), and Kuskov21 (Kuskov et al., 2021). The shaded triangle shows the composition range for which the solid Fe phase (+C at solid solubility limit) is expected to be in coexistence with Fe-C-S liquid. The dotted-dash curve is the miscibility gap at 5 GPa and 1873 K for Fe-C-S liquid alloys by Dasgupta et al. (2009). The same miscibility gap was assumed for the lower temperature in the absence of applicable data. Eutectic compositions for the Fe-S (Buono & Walker, 2011) and Fe-C (Fei & Brosh, 2014) binary systems at 5 GPa are also shown by the closed circles on the axes.

same trend of Fe-S liquids. As a first-order approximation, the limited substitution of sulfur with carbon (~18 at%) doesn't affect the local structure of the ternary liquid. However, the two elements have different quantitative effects on density and sound velocities (Figure 3). Indeed, S lowers both density and sound velocity of liquid iron more significantly than C, as readily visible from the experimental data of Fe-C and Fe-S liquids with the same atomic proportion. Nevertheless, density and/or sound velocity constrained by seismological or geodetical observations can still be used to address the carbon and sulfur content given in this thermodynamic model if both are present in the Moon's core.

Many Moon models were built by integrating various independent observables, including seismic, electromagnetic, geodetic, and geochemical data. Great efforts have been made to interpret these observables in terms of composition, but discrepancies still exist among studies, particularly concerning the core (Garcia et al., 2019; Kuskov et al., 2021; Viswanathan et al., 2019 and references therein). To discuss the possible content of sulfur and carbon in the Moon's core, two sets of density contours assuming a hotter (1850 K) and cooler (1600 K) core are plotted in Figure 4, where the densities proposed by three of the latest Moon models (see Table 3 and associated references for more details) are correlated with sulfur and carbon content based on here-presented results. In both cases, the Moon's core is assumed to be at 5 GPa. Note that in Kuskov et al. (2021), the Moon's core is modeled with a solid inner core surrounded by a liquid outer core, so that the solutions' space reported in Figure 4 corresponds to the C and S content in the outer core, while being not detectable by the LLR or seismological data, the existence of a solid inner core was deemed as uncertain by Garcia et al. (2019) and Viswanathan et al. (2019). Therefore, a homogenous liquid core was assumed in their studies.

Garcia et al. (2019) included two Moon models with the core density lower than that in Viswanathan et al. (2019) (hereafter Viswanathan19), resulting in a core prominently richer in sulfur. As the two models in Garcia et al. (2019) proposed quite similar core densities, the model 2 in that paper, hereafter Garcia19, using an updated geodetic data set, is taken for discussion here. As Fe, FeS, and Fe₃C were employed as end-members for the thermodynamic model, the mixing limit (i.e., the maximum light-element content) is defined by the curve linking FeS and Fe₃C in Figure 4. If this model were confirmed, the required sulfur content would range in 27–36 wt%, with the 250 K difference leading to a ~1 wt% shift in sulfur content, while the carbon content would be constrained by the ternary liquidus as a function of C and S content.

In the model Viswanathan19, the core oblateness as a function of radius was derived from two models, one with LLR-fitted polar MOI, and the other with a hydrostatic core model. The overlapped region indicates the core properties compatible with both models, which yield a core radius in the range of 381 ± 12 km with a density of 5,560–6,070 kg/m³. The proposed density and the corresponding C and S contents are shown in Figure 4. For a hotter core at

1850 K, carbon content spans from 0 to 4.6 wt%, approaching the miscibility gap (as our thermodynamic model is for a homogeneous liquid, the carbon content is not supposed to exceed this limit), and correspondingly, the sulfur content is constrained within 12–23 wt%. A colder core by 250 K would shift the contour to the S-richer side by ~1 wt% to balance the temperature effect.

The model Kuskov21 assumes a partially molten core of radius in the range 300–350 km. The favored densities of the liquid outer core and solid inner core are in the range of 6,200–7,000 kg/m³ and 7,500–7,700 kg/m³, respectively. The pseudobinary Fe(Ni)-S was considered in this paper, with a solid inner core composed of iron (plus

Table 3
Reference Models of the Moon's Core Here Considered for Discussion

	Garcia19	Viswanathan19	Kuskov21
Main data source	Seismic T_s , T_p Geodetic M , I/MR^2 , k_2 Electromagnetic ρ_a	Geodetic Lunar Laser Ranging data, k_2 Crustal thickness and density	Seismic T_s , T_p Geodetic M , I/MR^2 , k_2 Geochemical bulk concentration of FeO and Al ₂ O ₃
Core status	At least a liquid outer core ^a	At least a liquid outer core ^a	Solid inner core + liquid outer core
Density of the (outer) core	4,200–5,200 kg/m ³	5,560–6,070 kg/m ³	6,200–7,000 kg/m ³

Note. Garcia19 is from model 2 in Garcia et al. (2019); Viswanathan19 is from Viswanathan et al. (2019), and Kuskov21 is from model E in Kuskov et al. (2021).

^aThe presence or not of an inner core is not constrained.

nickel and light elements at trace level) and an outer liquid core made of Fe-S. We can then reconsider this model in the light of our results on the ternary Fe-C-S. Both Fe and Fe₃C are denser than the Fe-C-S liquids from which they crystallize and would be suitable candidates for an inner core, with the actual crystallizing phase controlled by the bulk concentration of carbon in the liquid.

1. For a bulk composition on the C-poor side (e.g., the Fe-0.33 wt% C-11.86 wt% S in Deng et al. (2013)), Fe would be the first crystallizing solid phase, leaving a Fe-C-S liquid outer core. Whether an Fe inner core would grow from the center (bottom-up) or Fe formed at the top of the core would snow across the liquid core (top-down) depends on total light element content, in particular the S content (Xu et al., 2021).
2. For a bulk composition with intermediate light element content (e.g., the Fe-5 wt% C-5 wt% S, see Dasgupta et al., 2009), Fe₃C would be the first solid phase to crystallize to form a solid inner core, leaving a Fe-C-S liquid outer core until the entire available C is consumed. As in case (1), S content is expected to largely control the top-down versus bottom-up crystallization regime.
3. For a bulk composition on C-rich side (e.g., the Fe-4.35 wt% C-7.85 wt% S, see Deng et al., 2013), graphite will first form during the core cooling process and float upward to the core-mantle boundary, followed by the crystallization of Fe₃C during the continuous temperature decrease to form an inner core. When applied to the model of Kuskov21, only the latter stage is considered. Case (3) can thus be brought back to case (2).

Measurements (Dasgupta et al., 2009; Deng et al., 2013) on the Fe-C-S ternary system have supported the above-outlined three crystallization regimes, which are strongly dependent on the bulk C and S content. We stress, however, that with a limited number of experiments conducted only with a few specific compositions, the C threshold between the C-poor and C-rich side, that is, the eutectic point, and how it modifies with sulfur content, remain poorly constrained.

A solid inner core of fcc-iron with a density of 7,500–7,700 kg/m³ was proposed in the model of Kuskov2021. In this case, further limits in the amounts of light elements, beside the above-mentioned eutectic, are placed by the liquidus (the existence of an inner core in equilibrium with melt imposes conditions below those at liquidus). Melting experiments in the Fe-S-C system indicate that the liquidus temperature decreases significantly compared to that in the Fe-S binary system by adding a very small amount of carbon into the Fe-S system (Deng et al., 2013). In the absence of precise determination of the phase diagram of the Fe-C-S system, the ternary composition at liquidus temperature of 1850 K (hot case) and 1600 K (cold case) are estimated as linear interpolation between results for the Fe-C and Fe-S binary systems and shown as shaded area in the Fe corner (Figure 4). The entire compositional space corresponding to the density of the outer core proposed in Kuskov21 lies outside this corner for a core at 1850 K. In other words, a relatively hot core at 1850 K could hardly support a solid inner core. If a colder core at 1600 K is assumed, the C and S content at liquidus are expected to significantly increase, enabling an overlap between the solutions in the compositional space accounting for the proposed outer core density and the existence of Fe inner core. In this case, the liquid outer core would have sulfur and carbon content ranging from 13 to 5 and from 0 to 2.3 wt%, respectively.

5. Conclusions

Liquid structures and densities of Fe-C-S alloys have been studied by a multi-technique approach at high pressure and high temperature, up to 5 GPa and 1900 K, over a large range of carbon and sulfur content. The experimental

data were employed to establish a non-ideal thermodynamic solution model for density and other thermo-elastic properties of liquid ternary alloys as a function of pressure and composition, which provides a useful database to discuss the composition of the core of small telluric planetary bodies.

Local structure, density and sound velocity of the ternary Fe-C-S liquids have been compared to those of binary Fe-C and Fe-S liquids. Although both interstitial, S and C affect the liquid structure differently, with $g(r)$ of ternary Fe-C-S liquid very close to the $g(r)$ of binary Fe-S liquid with the same light element content. At first approximation, the local structure of ternary liquids is thus controlled by the S content. Conversely, both density and sound velocity of ternary alloys show a co-effect of carbon and sulfur. With specific regard to density, values of ternary alloys are distributed between the upper and lower values provided by Fe-C and Fe-S alloys, respectively, having the same total amount of light elements. Still, the effect of S is more significant, lowering both density and sound velocities of the ternary Fe-C-S liquids with respect to pure Fe more significantly than C, as evident from the direct comparison of properties of ternary alloys with the same total amount of light elements but different C versus S proportions.

Based on the acquired knowledge of the thermo-elastic properties of Fe-C-S alloys, and the derived thermodynamic model, we discussed the simultaneous presence of carbon and sulfur in the Moon's core. Three of the latest Moon models have been considered, which propose different core states (fully molten vs. partially molten) and have quite different core densities, and thus light element content. Carbon, differently from sulfur, is hardly constrained on the sole basis of density and/or sound velocity. Assuming that the Moon's core is composed of a homogeneous Fe-C-S liquid, the specific carbon and sulfur content has been discussed on the basis of the two models assuming a fully molten core (Garcia et al., 2019; Viswanathan et al., 2019) at two reference temperatures, 1850 K and 1600 K. Derived sulfur content in the 12–23 wt% range (Viswanathan et al., 2019) or 27–36 wt% for model 2 in Garcia et al. (2019), well above upper limits proposed on the basis of core differentiation models (e.g., Rai and van Westrenen, 2014). This apparent incompatibility between a light, S-rich core advocated by geophysical observations and an S-poor core put forward by core-differentiation models, metal-silicate partitioning and elemental abundances in the bulk silicate Moon remains to be addressed. On the other hand, if the core were not fully molten (e.g., model E in Kuskov et al. (2021)), in the Fe-C-S system, a solid inner core would be made of Fe or Fe_3C depending on whether the bulk C content is on the C-poor or C-rich side of the eutectic. The currently limited knowledge of the phase diagram and melting properties of the ternary Fe-C-S system does not allow an entirely quantitative discussion. The existence of a solid inner core puts more constraints on the core's temperature since it must be below the liquidus. If we assume a core temperature of about 1850 K, the amounts of S and C required to match the outer core density proposed in model E by Kuskov et al. (2021) make the existence of a solid inner core rather unlikely. As the liquidus temperature at the Fe-rich side decreases with increasing S or C content, a cooler core can accommodate more light elements in the liquid outer core while having an fcc-Fe solid inner core, in qualitative agreement with the model of Kuskov21. Assuming a temperature of 1600 K, the sulfur and carbon content in the liquid outer core, in coexistence with an fcc-Fe (+C at solubility limit) inner core, would be 5–13 wt% and 2.7–0 wt% (the higher C content correlates with the lower S). However, for a solid inner core composed of Fe_3C , the light element budget in the liquid outer core strongly depends on a detailed understanding of the phase diagram and partial melting properties of the ternary Fe-C-S system, for which further studies are needed.

Acknowledgments

The authors wish to thank Imène Estève for her help with sample analysis by SEM, and Michel Fialin and Nicolas Rividi for their help during microprobe analysis. Yann Le Godec is acknowledged for fruitful discussions and his help for the definition and preparation of the PEC assembly. We also thank James Badro and Nicolas Wehr for preliminary tests conducted in piston cylinder press, Anat Shahar for kindly delivering our samples to the Earth and Planets Laboratory, Washington DC, and Emma Bullock for technical assistance. This project has received funding from the European Research Council (ERC) under the European Union's Horizon 2020 research and innovation Programme (Grant 724690). YF acknowledges NASA's support (80NSSC20K0337). The Scanning Electron Microscope (SEM) facility at IMPMC is supported by Région Ile de France Grant SESAME 2006 NoI-07-593/R, INSU-CNRS, Institut de Physique (INP)-CNRS, University Pierre et Marie Curie-Paris 6, and by the French National Re-search Agency (ANR) Grant ANR-07-BLAN-0124-01. The authors acknowledge synchrotron SOLEIL for the provision of beamtime under proposals 20191835 and 20210144.

Data Availability Statement

Raw experimental data and the Python and Matlab code for data analysis have been published in the Zenodo online repository (B. Zhao et al., 2022).

References

- Anderson, W. W., & Ahrens, T. J. (1994). An equation of state for liquid iron and implications for the Earth's core. *Journal of Geophysical Research*, 99(B3), 4273–4284. <https://doi.org/10.1029/93JB03158>
- Antonangeli, D., Morard, G., Schmerr, N. C., Komabayashi, T., Krisch, M., Fiquet, G., & Fei, Y. (2015). Toward a mineral physics reference model for the Moon's core. *Proceedings of the National Academy of Sciences*, 112(13), 3916–3919. <https://doi.org/10.1073/pnas.1417490112>
- Boccatto, S., Garino, Y., Morard, G., Zhao, B., Xu, F., Sanloup, C., et al. (2022). Amorpheus: A Python-based software for the treatment of X-ray scattering data of amorphous and liquid systems. *High Pressure Research*, 42(1), 69–93. <https://doi.org/10.1080/08957959.2022.2032032>
- Boulard, E., Denoual, C., Dewaele, A., King, A., Le Godec, Y., & Guignot, N. (2020). Following the phase transitions of iron in 3D with X-ray tomography and diffraction under extreme conditions. *Acta Materialia*, 192, 30–39. <https://doi.org/10.1016/j.actamat.2020.04.030>

- Boulard, E., King, A., Guignot, N., Deslandes, J. P., Le Godec, Y., Perrillat, J. P., et al. (2018). High-speed tomography under extreme conditions at the PSICHE beamline of the SOLEIL Synchrotron. *Journal of Synchrotron Radiation*, 25(3), 818–825. <https://doi.org/10.1107/S1600577518004861>
- Buono, A. S., & Walker, D. (2011). The Fe-rich liquidus in the Fe–FeS system from 1 bar to 10 GPa. *Geochimica et Cosmochimica Acta*, 75(8), 2072–2087. <https://doi.org/10.1016/j.gca.2011.01.030>
- Chen, J., Yu, T., Huang, S., Girard, J., & Liu, X. (2014). Compressibility of liquid FeS measured using X-ray radiograph imaging. *Physics of the Earth and Planetary Interiors*, 228, 294–299. <https://doi.org/10.1016/j.pepi.2013.12.012>
- Corgne, A., Wood, B. J., & Fei, Y. (2008). C- and S-rich molten alloy immiscibility and core formation of planetesimals. *Geochimica et Cosmochimica Acta*, 72(9), 2409–2416. <https://doi.org/10.1016/j.gca.2008.03.001>
- Dasgupta, R., Buono, A., Whelan, G., & Walker, D. (2009). High-pressure melting relations in Fe–C–S systems: Implications for formation, evolution, and structure of metallic cores in planetary bodies. *Geochimica et Cosmochimica Acta*, 73(21), 6678–6691. <https://doi.org/10.1016/j.gca.2009.08.001>
- Deng, L., Fei, Y., Liu, X., Gong, Z., & Shahar, A. (2013). Effect of carbon, sulfur and silicon on iron melting at high pressure: Implications for composition and evolution of the planetary terrestrial cores. *Geochimica et Cosmochimica Acta*, 114, 220–233. <https://doi.org/10.1016/j.gca.2013.01.023>
- Dickey, J. O., Bender, P. L., Faller, J. E., Newhall, X. X., Ricklefs, R. L., Ries, J. G., et al. (1994). Lunar laser ranging: A continuing legacy of the Apollo program. *Science*, 265(5171), 482–490. <https://doi.org/10.1126/science.265.5171.482>
- Eggert, J. H., Weck, G., Loubeyre, P., & Mezouar, M. (2002). Quantitative structure factor and density measurements of high-pressure fluids in diamond anvil cells by X-ray diffraction: Argon and water. *Physical Review B*, 65(17), 174105. <https://doi.org/10.1103/PhysRevB.65.174105>
- Fei, Y., Bertka, C. M., & Finger, L. W. (1997). High-pressure iron-sulfur compound, Fe₃S₂, and melting relations in the Fe–FeS system. *Science*, 275(5306), 1621–1623. <https://doi.org/10.1126/science.275.5306.1621>
- Fei, Y., & Brosh, E. (2014). Experimental study and thermodynamic calculations of phase relations in the Fe–C system at high pressure. *Earth and Planetary Science Letters*, 408, 155–162. <https://doi.org/10.1016/j.epsl.2014.09.044>
- Fei, Y., Li, J., Bertka, C. M., & Prewitt, C. T. (2000). Structure type and bulk modulus of Fe₃S, a new iron-sulfur compound. *American Mineralogist*, 85(11–12), 1830–1833. <https://doi.org/10.2138/am-2000-11-1229>
- Garcia, R. F., Gagnepain-Beyneix, J., Chevrot, S., & Lognonné, P. (2011). Very preliminary reference Moon model. *Physics of the Earth and Planetary Interiors*, 188(1–2), 96–113. <https://doi.org/10.1016/j.pepi.2011.06.015>
- Garcia, R. F., Khan, A., Drilleau, M., Margerin, L., Kawamura, T., Sun, D., et al. (2019). Lunar seismology: An update on interior structure models. *Space Science Reviews*, 215(8), 1–47. <https://doi.org/10.1007/s11214-019-0613-y>
- Henry, L., Guignot, N., King, A., Giovenco, E., Deslandes, J. P., & Itié, J. P. (2022). In situ characterization of liquids at high pressure combining X-ray tomography, X-ray diffraction and X-ray absorption using the white beam station at PSICHE. *Journal of Synchrotron Radiation*, 29(3), 853–861. <https://doi.org/10.1107/S1600577522003411>
- Hood, L. L., Mitchell, D. L., Lin, R. P., Acuna, M. H., & Binder, A. B. (1999). Initial measurements of the lunar induced magnetic dipole moment using Lunar Prospector magnetometer data. *Geophysical Research Letters*, 26(15), 2327–2330. <https://doi.org/10.1029/1999GL900487>
- Jing, Z., Wang, Y., Kono, Y., Yu, T., Sakamaki, T., Park, C., et al. (2014). Sound velocity of Fe–S liquids at high pressure: Implications for the Moon's molten outer core. *Earth and Planetary Science Letters*, 396, 78–87. <https://doi.org/10.1016/j.epsl.2014.04.015>
- Karato, S. I. (2013). Geophysical constraints on the water content of the lunar mantle and its implications for the origin of the Moon. *Earth and Planetary Science Letters*, 384, 144–153. <https://doi.org/10.1016/j.epsl.2013.10.001>
- Khan, A., MacLennan, J., Taylor, S. R., & Connolly, J. A. D. (2006). Are the Earth and the Moon compositionally alike? Inferences on lunar composition and implications for lunar origin and evolution from geophysical modeling. *Journal of Geophysical Research*, 111(E5), E05005. <https://doi.org/10.1029/2005JE002608>
- Kilburn, M. R., & Wood, B. J. (1997). Metal–silicate partitioning and the incompatibility of S and Si during core formation. *Earth and Planetary Science Letters*, 152(1–4), 139–148. [https://doi.org/10.1016/S0012-821X\(97\)00125-8](https://doi.org/10.1016/S0012-821X(97)00125-8)
- King, A., Guignot, N., Henry, L., Morard, G., Clark, A., Le Godec, Y., & Itié, J. P. (2022). Combined angular and energy dispersive diffraction: Optimized data acquisition, normalization and reduction. *Journal of Applied Crystallography*, 55(2), 218–227. <https://doi.org/10.1107/S1600576722000322>
- Konopliv, A. S., Binder, A. B., Hood, L. L., Kucinskas, A. B., Sjogren, W. L., & Williams, J. G. (1998). Improved gravity field of the Moon from Lunar Prospector. *Science*, 281(5382), 1476–1480. <https://doi.org/10.1126/science.281.5382.1476>
- Kuskov, O. L., & Belashchenko, D. K. (2016). Thermodynamic properties of Fe–S alloys from molecular dynamics modeling: Implications for the lunar fluid core. *Physics of the Earth and Planetary Interiors*, 258, 43–50. <https://doi.org/10.1016/j.pepi.2016.07.006>
- Kuskov, O. L., Kronrod, E. V., Matsumoto, K., & Kronrod, V. A. (2021). Physical properties and internal structure of the central region of the Moon. *Geochemistry International*, 59(11), 1018–1037. <https://doi.org/10.1134/S0016702921110069>
- Kuwabara, S., Terasaki, H., Nishida, K., Shimoyama, Y., Takubo, Y., Higo, Y., et al. (2016). Sound velocity and elastic properties of Fe–Ni and Fe–Ni–C liquids at high pressure. *Physics and Chemistry of Minerals*, 43(3), 229–236. <https://doi.org/10.1007/s00269-015-0789-y>
- Lai, X., Chen, B., Wang, J., Kono, Y., & Zhu, F. (2017). Polyamorphic transformations in Fe–Ni–C liquids: Implications for chemical evolution of terrestrial planets. *Journal of Geophysical Research: Solid Earth*, 122(12), 9745–9754. <https://doi.org/10.1002/2017JB014835>
- Lognonné, P., Gagnepain-Beyneix, J., & Chenet, H. (2003). A new seismic model of the Moon: Implications for structure, thermal evolution and formation of the Moon. *Earth and Planetary Science Letters*, 211(1–2), 27–44. [https://doi.org/10.1016/S0012-821X\(03\)00172-9](https://doi.org/10.1016/S0012-821X(03)00172-9)
- Lognonné, P., & Johnson, C. (2007). Planetary seismology. *Treatise on Geophysics*, 10, 69–122.
- Matsui, M., Ito, E., Katsura, T., Yamazaki, D., Yoshino, T., Yokoyama, A., & Funakoshi, K. i. (2009). The temperature–pressure–volume equation of state of platinum. *Journal of Applied Physics*, 105(1), 013505. <https://doi.org/10.1063/1.3054331>
- Matsui, M., Parker, S. C., & Leslie, M. (2000). The MD simulation of the equation of state of MgO: Application as a pressure calibration standard at high temperature and high pressure. *American Mineralogist*, 85(2), 312–316. <https://doi.org/10.2138/am-2000-2-308>
- Morard, G., Bouchet, J., Rivoldini, A., Antonangeli, D., Roberge, M., Boulard, E., et al. (2018). Liquid properties in the Fe–FeS system under moderate pressure: Tool box to model small planetary cores. *American Mineralogist: Journal of Earth and Planetary Materials*, 103(11), 1770–1779. <https://doi.org/10.2138/am-2018-6405>
- Morard, G., Garbarino, G., Antonangeli, D., Andraut, D., Guignot, N., Siebert, J., et al. (2014). Density measurements and structural properties of liquid and amorphous metals under high pressure. *High Pressure Research*, 34(1), 9–21. <https://doi.org/10.1080/08957959.2013.860137>
- Morard, G., Sanloup, C., Guillot, B., Fiquet, G., Mezouar, M., Perrillat, J. P., et al. (2008). In situ structural investigation of Fe–S–Si immiscible liquid system and evolution of Fe–S bond properties with pressure. *Journal of Geophysical Research*, 113(B10), B10205. <https://doi.org/10.1029/2008JB005663>

- Nakamura, Y. (2005). Farside deep moonquakes and deep interior of the Moon. *Journal of Geophysical Research*, *110*(E1), E01001. <https://doi.org/10.1029/2004JE002332>
- Nakamura, Y., Latham, G., Lammlein, D., Ewing, M., Duennebier, F., & Dorman, J. (1974). Deep lunar interior inferred from recent seismic data. *Geophysical Research Letters*, *1*(3), 137–140. <https://doi.org/10.1029/GL0011003p00137>
- Nishida, K., Ohtani, E., Urakawa, S., Suzuki, A., Sakamaki, T., Terasaki, H., & Katayama, Y. (2011). Density measurement of liquid FeS at high pressures using synchrotron X-ray absorption. *American Mineralogist*, *96*(5–6), 864–868. <https://doi.org/10.2138/am.2011.3616>
- Nishida, K., Shibazaki, Y., Terasaki, H., Higo, Y., Suzuki, A., Funamori, N., & Hirose, K. (2020). Effect of sulfur on sound velocity of liquid iron under Martian core conditions. *Nature Communications*, *11*(1), 1954. <https://doi.org/10.1038/s41467-020-15755-2>
- Nishida, K., Suzuki, A., Terasaki, H., Shibazaki, Y., Higo, Y., Kuwabara, S., et al. (2016). Towards a consensus on the pressure and composition dependence of sound velocity in the liquid Fe–S system. *Physics of the Earth and Planetary Interiors*, *257*, 230–239. <https://doi.org/10.1016/j.pepi.2016.06.009>
- Nishida, K., Terasaki, H., Ohtani, E., & Suzuki, A. (2008). The effect of sulfur content on density of the liquid Fe–S at high pressure. *Physics and Chemistry of Minerals*, *35*(7), 417–423. <https://doi.org/10.1007/s00269-008-0236-4>
- O'Neill, H. S. C. (1991). The origin of the Moon and the early history of the Earth—A chemical model. Part 1: The Moon. *Geochimica et Cosmochimica Acta*, *55*(4), 1135–1157. [https://doi.org/10.1016/0016-7037\(91\)90168-5](https://doi.org/10.1016/0016-7037(91)90168-5)
- Parker, M., Sanloup, C., Tronche, E. J., Perrillat, J. P., Mezouar, M., Rai, N., & van Westrenen, W. (2010). Calibration of a diamond capsule cell assembly for in situ determination of liquid properties in the Paris–Edinburgh press. *High Pressure Research*, *30*(2), 332–341. <https://doi.org/10.1080/08957959.2010.484283>
- Pommier, A., Driscoll, P. E., Fei, Y., & Walter, M. J. (2022). Investigating metallic cores using experiments on the physical properties of liquid iron alloys. *Frontiers in Earth Science*, *10*, 956971. <https://doi.org/10.3389/feart.2022.956971>
- Rai, N., & van Westrenen, W. (2014). Lunar core formation: New constraints from metal–silicate partitioning of siderophile elements. *Earth and Planetary Science Letters*, *388*, 343–352. <https://doi.org/10.1016/j.epsl.2013.12.001>
- Ricolleau, A., Fei, Y., Corgne, A., Siebert, J., & Badro, J. (2011). Oxygen and silicon contents of Earth's core from high pressure metal–silicate partitioning experiments. *Earth and Planetary Science Letters*, *310*(3–4), 409–421. <https://doi.org/10.1016/j.epsl.2011.08.004>
- Sanloup, C., Guyot, F., Gillet, P., Fiquet, G., Mezouar, M., & Martinez, I. (2000). Density measurements of liquid Fe–S alloys at high-pressure. *Geophysical Research Letters*, *27*(6), 811–814. <https://doi.org/10.1029/1999GL008431>
- Sanloup, C., Van Westrenen, W., Dasgupta, R., Maynard-Casely, H., & Perrillat, J. P. (2011). Compressibility change in iron-rich melt and implications for core formation models. *Earth and Planetary Science Letters*, *306*(1–2), 118–122. <https://doi.org/10.1016/j.epsl.2011.03.039>
- Shibazaki, Y., & Kono, Y. (2018). Effect of silicon, carbon, and sulfur on structure of liquid iron and implications for structure-property relations in liquid iron-light element alloys. *Journal of Geophysical Research: Solid Earth*, *123*(6), 4697–4706. <https://doi.org/10.1029/2018JB015456>
- Shibazaki, Y., Kono, Y., & Fei, Y. (2015). Microscopic structural change in a liquid Fe–C alloy of ~5 GPa. *Geophysical Research Letters*, *42*(13), 5236–5242. <https://doi.org/10.1002/2015GL064271>
- Shimizu, H., Matsushima, M., Takahashi, F., Shibuya, H., & Tsunakawa, H. (2013). Constraint on the lunar core size from electromagnetic sounding based on magnetic field observations by an orbiting satellite. *Icarus*, *222*(1), 32–43. <https://doi.org/10.1016/j.icarus.2012.10.029>
- Shimoyama, Y., Terasaki, H., Ohtani, E., Urakawa, S., Takubo, Y., Nishida, K., et al. (2013). Density of Fe–3.5 wt% C liquid at high pressure and temperature and the effect of carbon on the density of the molten iron. *Physics of the Earth and Planetary Interiors*, *224*, 77–82. <https://doi.org/10.1016/j.pepi.2013.08.003>
- Shimoyama, Y., Terasaki, H., Urakawa, S., Takubo, Y., Kuwabara, S., Kishimoto, S., et al. (2016). Thermoelastic properties of liquid Fe–C revealed by sound velocity and density measurements at high pressure. *Journal of Geophysical Research: Solid Earth*, *121*(11), 7984–7995. <https://doi.org/10.1002/2016JB012968>
- Steinstra, E. S., Lin, Y., Rai, N., Jansen, M., & van Westrenen, W. (2017). Carbon as the dominant light element in the lunar core. *American Mineralogist*, *102*(1), 92–97. <https://doi.org/10.2138/am-2017-5727>
- Terasaki, H., Nishida, K., Shibazaki, Y., Sakamaki, T., Suzuki, A., Ohtani, E., & Kikegawa, T. (2010). Density measurement of Fe₃C liquid using X-ray absorption image up to 10 GPa and effect of light elements on compressibility of liquid iron. *Journal of Geophysical Research*, *115*(B6), B06207. <https://doi.org/10.1029/2009JB006905>
- Terasaki, H., Rivoldini, A., Shimoyama, Y., Nishida, K., Urakawa, S., Maki, M., et al. (2019). Pressure and composition effects on sound velocity and density of core-forming liquids: Implication to core compositions of terrestrial planets. *Journal of Geophysical Research: Planets*, *124*(8), 2272–2293. <https://doi.org/10.1029/2019JE005936>
- Toksöz, M. N., Dainty, A. M., Solomon, S. C., & Anderson, K. R. (1974). Structure of the Moon. *Reviews of Geophysics*, *12*(4), 539–567. <https://doi.org/10.1029/RG012i004p00539>
- Tsuno, K., Frost, D. J., & Rubie, D. C. (2011). The effects of nickel and sulphur on the core–mantle partitioning of oxygen in Earth and Mars. *Physics of the Earth and Planetary Interiors*, *185*(1–2), 1–12. <https://doi.org/10.1016/j.pepi.2010.11.009>
- Viswanathan, V., Rambaux, N., Fienga, A., Laskar, J., & Gastineau, M. (2019). Observational constraint on the radius and oblateness of the lunar core–mantle boundary. *Geophysical Research Letters*, *46*(13), 7295–7303. <https://doi.org/10.1029/2019GL082677>
- Weber, R. C., Lin, P. Y., Garnero, E. J., Williams, Q., & Lognonné, P. (2011). Seismic detection of the lunar core. *Science*, *331*(6015), 309–312. <https://doi.org/10.1126/science.1199375>
- Wieczorek, M. A., Jolliff, B. L., Khan, A., Pritchard, M. E., Weiss, B. P., Williams, J. G., et al. (2006). The constitution and structure of the lunar interior. *Reviews in Mineralogy and Geochemistry*, *60*(1), 221–364. <https://doi.org/10.2138/rmg.2006.60.3>
- Williams, J. G., Konopliv, A. S., Boggs, D. H., Park, R. S., Yuan, D. N., Lemoine, F. G., et al. (2014). Lunar interior properties from the GRAIL mission. *Journal of Geophysical Research: Planets*, *119*(7), 1546–1578. <https://doi.org/10.1002/2013JE004559>
- Xu, F., Morard, G., Guignot, N., Rivoldini, A., Manthilake, G., Chantel, J., et al. (2021). Thermal expansion of liquid Fe–S alloy at high pressure. *Earth and Planetary Science Letters*, *563*, 116884. <https://doi.org/10.1016/j.epsl.2021.116884>
- Zhao, B., Morard, G., Boulard, E., Boccato, S., Siersch, N., Rivoldini, A., et al. (2022). Local structure and density of liquid Fe–C–S alloys at Moon's core conditions [Dataset]. Zenodo. <https://doi.org/10.5281/zenodo.7030984>
- Zhao, Y., Von Drele, R. B., Weidner, D. J., & Schiferl, D. (1997). P–V–T Data of hexagonal boron nitride h BN and determination of pressure and temperature using thermoelastic equations of state of multiple phases. *International Journal of High Pressure Research*, *15*(6), 369–386. <https://doi.org/10.1080/08957959708240481>

References From the Supporting Information

- Chantler, C. T., Olsen, K., Dragoset, R. A., Chang, J., Kishore, A. R., Kotochigova, S. A., & Zucker, D. S. (2005). *Detailed tabulation of atomic form factors, photoelectric absorption and scattering cross section, and mass attenuation coefficients for Z = 1–92 from E = 1–10 eV to E = 0.4–1.0 MeV*. NIST. Physical Measurement Laboratory. <https://doi.org/10.18434/T4HS32>
- Hubbell, J. H., & Seltzer, S. M. (2004). *Tables of X-Ray mass attenuation coefficients and mass energy-absorption coefficients from 1 keV to 20 MeV for elements Z = 1 to 92 and 48 additional substances of dosimetric interest*. Radiation Physics Division, PML, NIST. <https://doi.org/10.18434/T4D01F>
- Knibbe, J. S., Rivoldini, A., Luginbuhl, S. M., Namur, O., Charlier, B., Mezouar, M., et al. (2021). Mercury's interior structure constrained by density and P-wave velocity measurements of liquid Fe-Si-C alloys. *Journal of Geophysical Research: Planets*, 126(1), e2020JE006651. <https://doi.org/10.1029/2020JE006651>
- Komabayashi, T. (2014). Thermodynamics of melting relations in the system Fe-FeO at high pressure: Implications for oxygen in the Earth's core. *Journal of Geophysical Research: Solid Earth*, 119(5), 4164–4177. <https://doi.org/10.1002/2014JB010980>